



3D printing of living structural biocomposites

Matteo Hirsch^{1,†}, Lorenzo Lucherini^{1,†}, Ran Zhao¹, Alexandra Clarà Saracho², Esther Amstad^{1,*}

¹ Soft Materials Laboratory, Institute of Materials, École Polytechnique Fédérale de Lausanne, 1015 Lausanne, Switzerland

² Department of Engineering, University of Cambridge, Cambridge, United Kingdom

Nature fabricates organic/inorganic composites under benign conditions, yet, in many cases, their mechanical properties exceed those of the individual building components it is made from. The secret behind the evolutionary pivot is the unique ability of nature to control structure and local composition of its materials. This tight control is often achieved through compartmentalization of the reagents that can be locally released. Inspired by nature, we introduce an energy-efficient process that takes advantage of the compartmentalization to fabricate porous CaCO₃-based composites exclusively comprised of nature-derived materials whose compressive strength is similar to that of trabecular bones. The unique combination of nature-derived materials, 3D printability, and good mechanical properties is achieved through the formulation of these materials: We combine microgel-based granular inks that inherently can be 3D printed with the innate potential of engineered living materials to fabricate bacteria-induced biomineral composites. The resulting biomineral composites possess a porous trabecular structure that comprises up to 93 wt% CaCO₃ and thereby can withstand pressures up to 3.5 MPa. We envisage this system to have the potential to be used in art restoration, serve as artificial corals to help the regeneration of marine reefs, and, with additional work, might even allow the repair of broken or partially disintegrated natural mineral-based materials such as certain parts of bones.

Keywords: Microgel; Hydrogel; 3D printing; Microbially-induced calcium carbonate precipitation; Mineralization

Introduction

Nature is able to produce biocomposites of high structural complexity and mechanical integrity using a limited number of elements. These biocomposites are often fabricated under benign conditions and with a minimum amount of energy input [1]. The unparalleled mechanical properties of natural materials result from the unique interplay between hierarchical structure and locally varying composition [2]. Calcium carbonate-based

materials such as nacre [3], sea urchin spikes [4], and stomatopod dactyl clubs [5] represent a paradigmatic example of strong and tough natural biocomposites containing biominerals with well-defined orientations, structures, and compositions [6]. For example, 95% of the weight of nacre can be assigned to hexagonal aragonite platelets that are assembled in a layered structure. These inorganic platelets are held together by a polymeric matrix that increases the overall material toughness up to 40-fold compared to platelets alone [7–9]. In contrast, synthetic composites lack any micrometer length-scale structure because most of them are fabricated by mixing materials possessing different mechani-

* Corresponding author.

E-mail address: Amstad, E. (esther.amstad@epfl.ch)

† These authors contributed equally to the work.

cal properties in bulk [10,11]. Despite the higher energy cost of the production of most synthetic composites, the combination of stiffness and toughness remains unmatched by synthetic counterparts possessing a similar composition. This shortcoming can at least partially be assigned to the inferior control over the microstructure and local composition of synthetic materials [12,13].

Inspired by nature, techniques that offer a superior control over the local composition and hence result in composites with superior mechanical properties have been introduced. These methods include reinforcing composites with ions [14–16] or particle-based fillers [17–19], controlling the mineralization through enzymes [20–22], *in situ* precipitation of minerals [23–26], or layer-by-layer depositions [27,28]. Similarly, additive manufacturing methods that offer control over the mm length scale structure have been introduced [29–32]. However, by analogy to the bulk methods mentioned above, many of these more involved procedures offer a limited control over the micrometer length scale structure of the materials that negatively impacts their mechanical properties. Sustainable solutions to fabricate stiff and strong composites under benign conditions and using minimal amounts of energy remain elusive [33].

The introduction of engineered living materials presented a paradigm shift in the biocomposite field from the design of synthetic, inert biomaterials to biologically-active, self-growing ones. Recent studies have demonstrated the possibility to combine conventional geotechnical processing with a microbially-induced calcium carbonate precipitation (MICP) for the mechanical stabilization and reinforcement of soil [34,35], and for the production of self-healing concrete [36,37]. This combination has been possible because of the simplicity and high efficiency of the MICP process [38]. MICP by urea hydrolysis has also been demonstrated in the context of living construction materials [39], heritage restoration [40], and deep-seabed applications [41]. Generally, ureolytic bacteria used for such geo-environmental and construction applications must have a reliable, high urease activity, while being harmless to humans and pose low risk to the local ecosystem. *Sporosarcina pasteurii* has been often selected owing to its high-urease activity and biosafety [42]. Similarly, microorganisms have been embedded in soft organic materials to form engineered living materials [39,43,44]. For instance, bioinks have been supplemented with unicellular green algae to enable the 3D printing of cellular scaffolds displaying a homogeneous degree of oxygenation [45]. Similarly, hydrogel-based inks have been functionalized with bacteria that degrade phenolic compounds for bioremediation and those that produce bacterial cellulose for biomedical applications [46].

Bacteria have also been used to precipitate inorganic materials into organic matrices. For example, 3D printed acrylate-based, inert polymeric structures have been exposed to a MICP environment to trigger the precipitation of calcite within the empty space of the printed mesh. The formed calcite particles served as fillers, thereby increasing the stiffness and strength of the composite [47]. Yet, to achieve this effect, the composite had to be annealed at 70 °C.

Recent advances in additive manufacturing of cell-laden inks have highlighted the unparalleled printing potential of granular

systems over their conventional biopolymer counterparts [48–50]. However, the advantages offered by granular systems in terms of their processability have never been leveraged to 3D print bacteria-loaded biosourced materials that can subsequently be stiffened and strengthened through a controlled bacteria-initiated mineralization of the organic scaffold.

Here, we introduce a method that enables 3D printing of bacteria-loaded microgels, which can be converted into biomineral composites possessing up to 93 wt% CaCO₃ and bearing loads up to 3.5 MPa. This is achieved by fabricating gelatin microgels containing ureolytic bacteria, *Sporosarcina pasteurii*. These microgels are jammed to form a 3D printable granular bioink (BactoInk) that can be converted into load-bearing biocomposites through microbially-induced calcium carbonate precipitation. We obtain a homogeneous mineralization within microstructured composites with dimensions as large as 10 cm and mineral contents up to 93 wt%. We demonstrate that the compressive strength increases with the degree of mineralization until it attains values as high as 3.5 MPa, similar to those of the human trabecular bone [51]. The potential and versatility of the environmentally friendly BactoInk to be 3D printed into cm-sized statues, injected into defects for art restoration and cast into artificial corals that might help restoring marine reefs is showcased.

Results and discussion

Hydrogels display a striking similarity to naturally-produced extracellular matrices and biofilms. This similarity made hydrogels attractive for the encapsulation of microorganisms in the form of films [52], particles [39,53,54], capsules [55], fibers [56,57], and bulk structures [58,59]. Extrusion-based 3D printing of hydrogels is limited to those made of precursor solutions that fulfill the rheological requirements inherent to this process [60,61]. Unfortunately, these hydrogels typically are rather soft or fragile [62]. A much wider range of hydrogels can be 3D printed if formulated as microparticles, so-called microgels, that are jammed [48,50,63–65]. Yet, microgels that were thus far 3D printed did not contain microorganisms that precipitate materials which can change the mechanical properties of the resulting composite such that they were inherently soft [50,53,66]. To overcome this limitation and enable 3D printing of stiff biominerals from soft microgel-based inks, we produce microgels that are loaded with bacteria which can induce CaCO₃ precipitation. Due to its high urease activity and biosafety, we chose *S. pasteurii* as our bacteria.

Microgels must be biocompatible, solidify under conditions compatible with bacteria and jam if up-concentrated to enable 3D printing. Agarose proved to be too soft such that it could not be properly jammed, preventing a controlled 3D printing of this material, as shown in **Fig. S1**. By contrast, gelatin-based microparticles satisfied all the requirements such that we chose this biopolymer as a model system. We produce bacteria-loaded microgels by dispersing freeze-dried *S. pasteurii* in a gelatin solution at 37 °C, emulsifying the aqueous solution with mineral oil under vigorous stirring, and cooling the emulsion to room temperature. The resulting microgels are washed several times with phosphate buffered saline (PBS) to remove the oil and any unre-

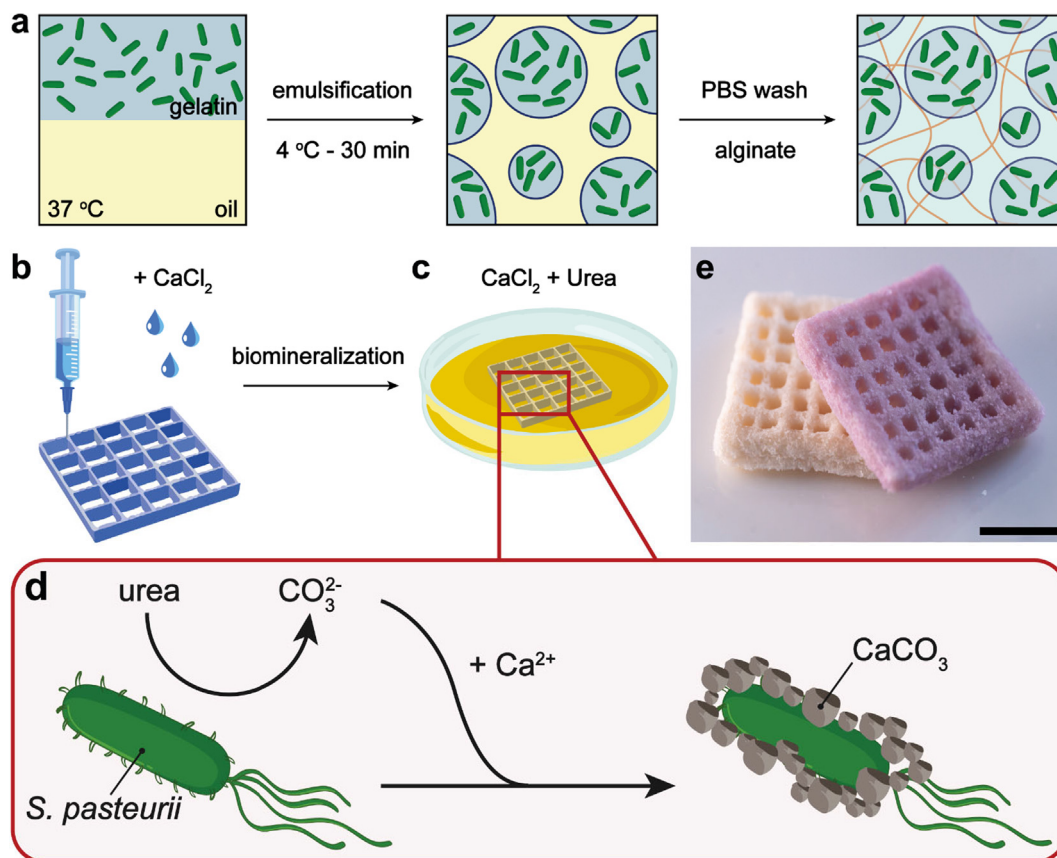


FIGURE 1

Fabrication of 3D printed biomineral composites. **a**, Schematic representation of the manufacturing process of the BactoInk. A gelatin solution containing bacteria is emulsified, the aqueous drops converted into microgels by lowering the temperature and the resulting microgels washed to remove the oil and surfactants. The bacteria-loaded microgels are mixed with a solution containing alginate prior to jamming. **b**, The BactoInk is 3D printed and the structure stabilized by exposure to a 1 M CaCl_2 solution. **c**, Mineralization is triggered by immersing the stabilized BactoInk scaffold in a solution containing 0.5 M CaCl_2 , 0.75 M urea, and 0.4 wt% yeast. **d**, Schematic representation of the MICP process mediated by *S. pasteurii*. **e**, Photograph of a 3D printed biomineral composite after 4 days of MICP. Scale bar is 10 mm.

acted moieties before they are resuspended in a solution containing alginate that serves as a stabilizer for our printed scaffolds, as summarized in Fig. 1a. The suspended bacteria-loaded microgels are jammed by centrifugation yielding our BactoInk.

Granular hydrogels typically suffer from weak inter-particle interactions that compromise their shape fidelity. To stabilize the structure, we add alginate and Ca^{2+} to the formulation; alginate starts to gel in the presence of Ca^{2+} . Alginate adds an additional benefit: It serves as a Ca^{2+} reservoir, thereby facilitating localized growth of CaCO_3 inside the 3D printed scaffold [67,68]. The resulting polymeric scaffold is soft, yet self-sustaining, as shown in Fig. 1b. To stiffen and harden the 3D printed structure, we trigger the MICP process by transferring the structure to a mineralizing environment containing yeast extract, urea, and CaCl_2 , as shown in Fig. 1c. The encapsulated *S. pasteurii* hydrolyze urea, leading to the formation of carbonate ions (CO_3^{2-}) that react with calcium ions (Ca^{2+}), which are dispersed in the solution to precipitate CaCO_3 minerals in the vicinity of the bacteria, as schematically shown in Fig. 1d. The resulting CaCO_3 minerals, that are formed within the 3D printed granular hydrogel scaffold, transform this soft scaffold into a

load-bearing biomineral composite, as illustrated on the photographs in Fig. 1e.

The rheological behavior of granular inks is independent of the material composition [49,69]. To verify that the addition of bacteria to microgels does not significantly change the rheological properties of the granular ink, we perform oscillatory rheology on our samples and compare the results to gelatin-only microgels. As expected, both inks are shear-thinning with no significant difference in viscosity, as shown in Fig. 2a. Additionally, both materials display a relatively low yield point of around 1 kPa, as shown in Fig. 2b, making them well suited for bioprinting. The moderately higher storage modulus (G') of the BactoInk is assigned to the presence of bacteria within the microgels that act as fillers, thereby stiffening them [70].

To ensure good printing resolution, the BactoInk should extrude into filaments in a continuous flow. To test if this prerequisite is met by our system, we investigate the influence of the concentration of gelatin within the microgels on the printability. Gelatin concentrations below 20 wt% yield microgels that are too soft to be sufficiently jammed such that the resulting ink drips, as shown in the photograph in Fig. 2c, and summarized

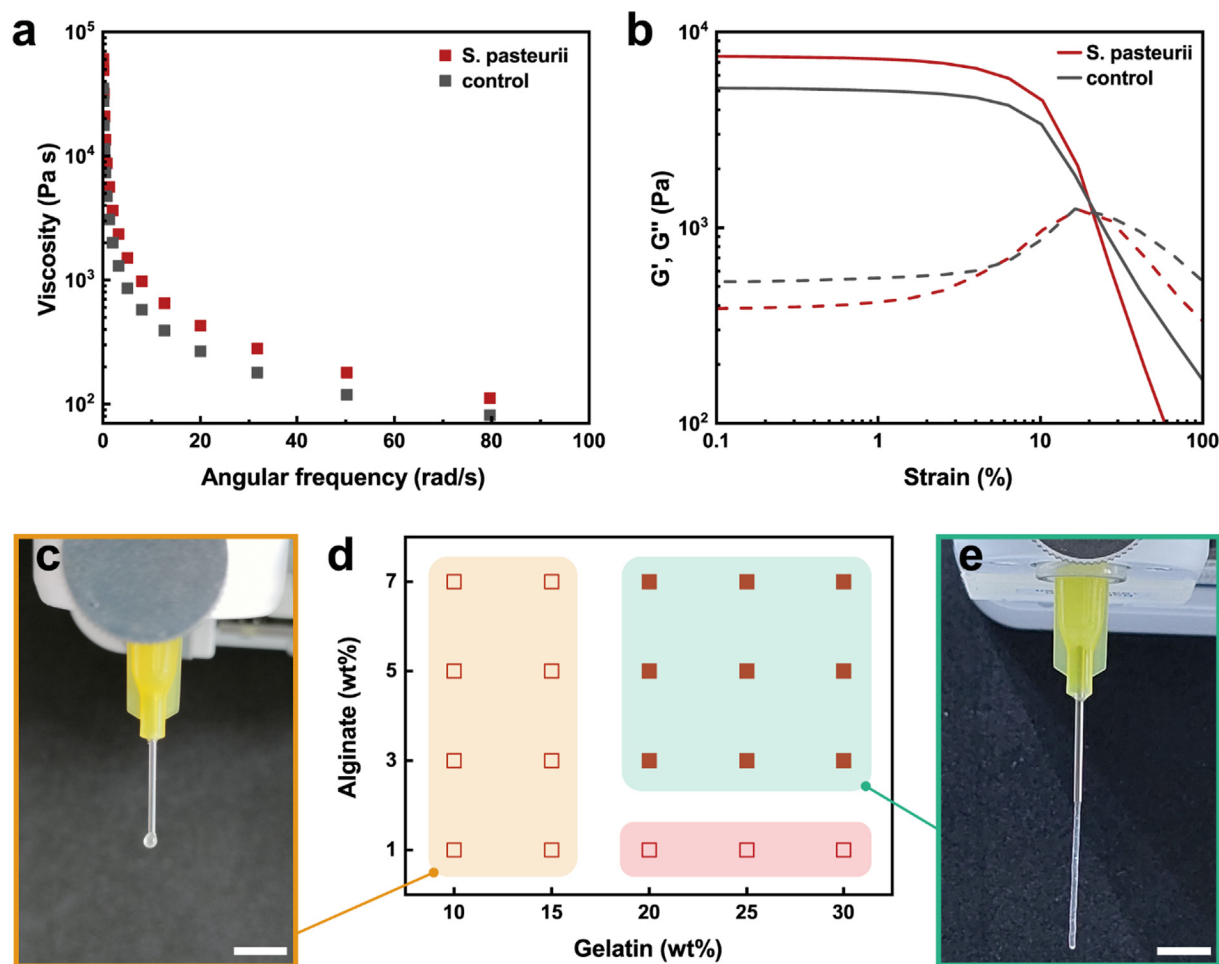


FIGURE 2

Rheology of Bactolnk. **a**, Frequency dependent viscosity of jammed bacteria-loaded microgels (red) versus bare gelatin microgels (grey). Both inks display a shear-thinning behavior. **b**, Amplitude sweep of Bactolnk (red) versus bare gelatin microgels (grey). Despite the moderate difference in G' , both inks show a similar flow point. **c**, Photograph of Bactolnk composed of jammed microparticles made from a solution containing 15 wt% gelatin dispersed in an aqueous solution containing 5 wt% alginate dripping from a nozzle. **d**, Bactolnk printability window as a function of gelatin and alginate concentrations. **e**, Photograph of Bactolnk made of jammed microparticles that have been fabricated from a solution containing 25 wt% gelatin dispersed in an aqueous solution containing 5 wt% alginate which extrudes in a stable filament. At gelatin concentrations below 20 wt%, the ink is too soft such that a proper jamming cannot be obtained and the material displays a dripping behavior, as exemplified in (c). At gelatin concentrations exceeding 20 wt%, all the tested formulations show a continuous filament extrusion such that they are suitable for 3D printing, as exemplified in (e). Alginate concentrations above 3 wt% are required to successfully stabilize the 3D printed structure upon exposure to CaCl_2 that forms a percolating alginate network, which firmly interconnects the microparticles. Scale bars are 5 mm.

in Fig. 2d. This behavior prevents printing of the ink. Microgels that are formulated from solutions containing gelatin concentrations exceeding 20 wt% display a proper jamming behavior. As a result, ink formulations made from these microgels can be 3D printed. Indeed, these formulations display a filament spreading as low as 13%, as shown in Fig. S2. Importantly, jammed microgels can be printed independent of the alginate concentration, as exemplified on the photograph in Fig. 2e for inks made with microgels composed of 25 wt% gelatin.

To enable the transfer of the 3D printed construct into a mineralizing solution, the structure must be free-standing and support its own weight. To test the influence of the alginate concentration around the microgels on the shape-retaining properties of our material, we perform a filament hanging assay. If the alginate content in the solution surrounding the micropar-

ticles is below 3 wt%, the inter-particle adhesion is too weak even upon contact with a CaCl_2 solution, such that the printed structure is not self-sustaining. By contrast, at higher alginate concentrations, the 3D printed structure becomes self-sustaining as soon as it has been exposed to a CaCl_2 solution, as shown in Fig. S3 and Movie M1. We assign the good stability of the 3D printed substrate to the alginate that gels upon contact with Ca^{2+} , thereby firmly connecting adjacent microparticles. Based on these findings, we use the Bactolnk composed of microgels made from solutions containing 25 wt% gelatin that are dispersed in an aqueous solution containing 5 wt% alginate for the following experiments.

The CaCO_3 precipitation yield is dependent on the relative concentrations of urea and CaCl_2 in solution, as well as on the time of exposure to the mineralizing solution [39]. To test the

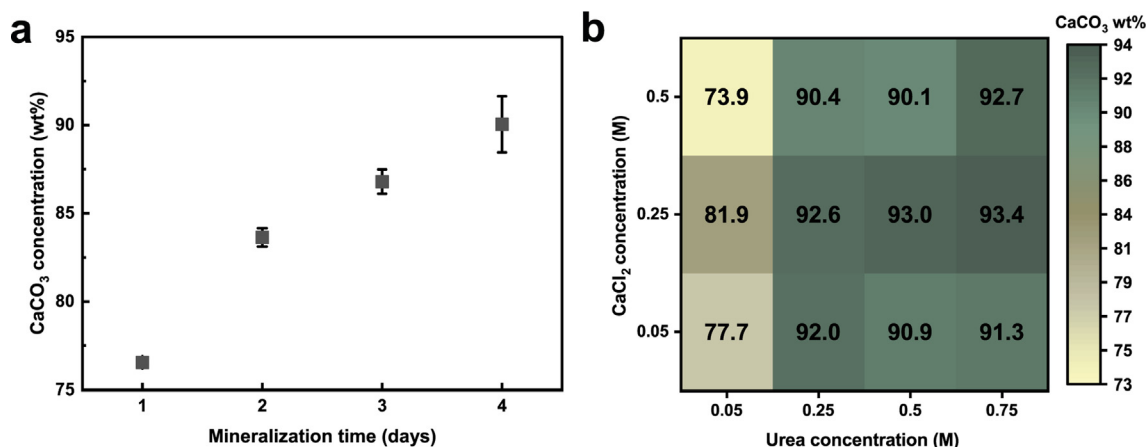


FIGURE 3

Mineralization. CaCO₃ content of biomaterialized Bactolnk determined with TGA as a function of **a**, mineralization time for samples incubated in an aqueous solution containing 0.5 M CaCl₂ and 0.75 M urea and **b**, different CaCl₂ and urea concentrations measured after 4 days of incubation at room temperature.

evolution of the mineral content over time, we quantify this parameter using thermogravimetry analysis (TGA). To minimize the amount of energy needed to fabricate these materials, we incubate the soft substrates at room temperature. The degree of mineralization gradually increases within 4 days of incubation, as shown in Fig. 3a. If samples are incubated in a solution containing 0.75 M urea and 0.5 M CaCl₂, they reach a mineral content up to 93 wt% after 4 days, as summarized in Fig. 3a. To test if we can increase the mineral content even more, we assess the influence of the urea concentration on the degree of mineralization measured after 4 days of incubation. The degree of mineralization increases up to 20% if the urea concentration is increased from 0.05 M to 0.25 M, independent of the CaCl₂ concentration, as summarized in Fig. 3b. By contrast, for urea concentrations ≥ 0.25 M, we do not observe any significant influence of the urea or CaCl₂ concentrations on the degree of mineralization, as summarized in Fig. 3b. These results suggest that the mineralization process is limited by the concentration of urea in the mineralizing solution, and hence by the available carbonate ions. To ensure maximum yield of the precipitated CaCO₃, we choose a solution containing 0.75 M urea and 0.5 M CaCl₂.

To evaluate the effect of the incubation time on the overall CaCO₃ mineral content, we perform TGA on the biomaterialized samples as a function of incubation days. Remarkably, bacteria produce up to 77 wt% of CaCO₃ within 24 h, and up to 93 wt% after 4 days of incubation, as shown in Fig. 3a. This high mineral content is surprising as we start from a purely organic scaffold that contains approximately 30 wt% of polymers. Assuming that all the volume initially occupied by water is replaced by CaCO₃, we would expect a maximum mineral content of 86 wt%. The measured mineralization value is higher than the theoretically calculated upper limit. This result suggests that a fraction of the polymer initially contained within the scaffold is degraded or washed away during the mineralization.

Some bacteria are known to metabolize small peptides and proteins, including gelatin, leading to the secretion of gelatinase [71]. To test whether *S. pasteurii* degrades and metabolizes the

gelatin scaffold, we monitor the change in microgel structure and pH with time. To facilitate the visualization, we perform these tests on individually dispersed bacteria-loaded microgels. In the absence of urea, bacteria-loaded microgels are stable and do not degrade over time, as shown in Fig. S4a. These results suggest that *S. pasteurii* do not possess the enzymatic capacity to hydrolyze and degrade gelatin. By contrast, in the presence of urea, gelatin microgels lose their integrity and bacteria are no longer encapsulated, as exemplified in the time-lapse optical micrographs in Fig. S4b. We assign this observation to the increase in pH from 6.5 to 10 caused by the urea hydrolysis, as shown in Fig. S4c. The zwitterionic nature of gelatin helices makes its structural integrity pH-dependent, leading to a partial disintegration at pH values exceeding 9 [72]. These results suggest that the gelatin microgels partially disintegrate during the mineralization of the scaffold, allowing the mineral content to increase beyond the maximum theoretical value. Importantly, the gelatin dissolution does not compromise the printing fidelity or resolution as this process happens only after the surfaces of the microgels have been mineralized, as shown in Fig. S4d.

A key parameter that determines the quality of a 3D printed construct is its shape fidelity. To assess if this parameter is impacted by the mineralization of the scaffold, that occurs after the 3D printing process has been completed, we compute the volume change of 3D printed parts upon drying as a function of the mineralization time, assuming a negligible volume change of fully mineralized materials upon their drying. As expected, the dried hydrogel scaffold loses more than 80% of its initial volume due to water evaporation, as shown in Fig. 4a. This large change in volume severely compromises the shape fidelity. Moreover, the dried product becomes very brittle, making it unsuitable for any further operation. Remarkably, after only 24 h of mineralization, the volume loss is much smaller, 20%. This result suggests that within 24 h, minerals form an interconnected structure that prevents the 3D printed parts from collapsing. The change in volume decreases further with mineralization time until at day 4, we observe an increase in volume of 10%, suggesting the onset of an

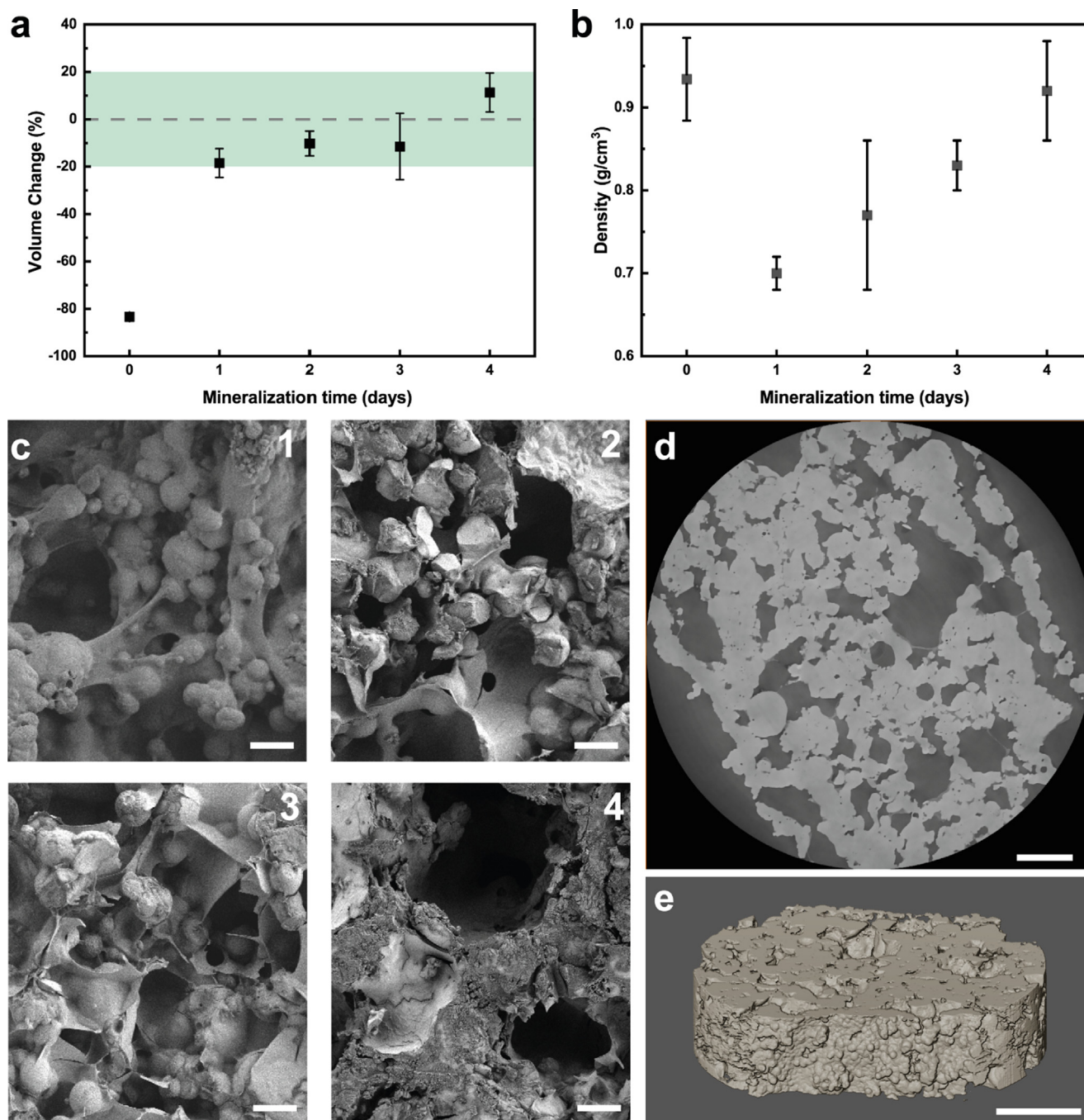


FIGURE 4

Biomaterial composite structural analysis. **a**, Volume change of dried 3D printed biomaterialized Bactolnk as a function of time. At day 0, in the absence of biomaterials, the structure collapses upon drying such that it loses 80% of its initial volume. The shrinkage upon drying strongly decreases with mineralization time. After 4 days of mineralization, an increase in volume is measured, indicating that the scaffold is over-mineralized. **b**, Density change as a function of mineralization time. In the absence of biomaterials, the dried polymeric scaffold possesses a dense structure. After 24 h of mineralization, the density of the scaffold decreases, suggesting the presence of a large fraction of pores. As the mineralization progresses, a steady increase in density is observed. **c**, SEM micrographs of biomaterialized scaffolds as a function of time. After 24 h of mineralization, biomaterials and the polymer scaffold co-exist. As the mineralization progresses, the polymer content decreases. After 4 days of mineralization, the individual mineralized particles are fused together forming mineral bridges. Scale bars are 100 μm . **d-e**, **(d)** μCT scan and **(e)** 3D reconstruction of a biomaterialized scaffold after 4 days of mineralization. The cross-section reveals a trabecular structure with a relative porosity of 47 vol%. Scale bar in **(d)** is 250 μm , and **(e)** is 500 μm .

over-mineralization of the structure. To avoid a strong over-mineralization, which would compromise the shape fidelity, we stop the mineralization of our scaffolds after 4 days. Note that

over-mineralization could also be prevented by reducing the urea concentration, lowering the solution pH, or immersing the sample in ethanol to quench the bacteria activity.

Our results indicate that within 24 h of incubation, the minerals form an interconnected network that gradually densifies within the next 72 h of incubation. To test this suggestion, we quantify the change in density of the composite over time. After 24 h of mineralization the composite density is as low as 0.7 g/cm³, as shown in Fig. 4b. This result suggests that the mineral has already formed an interconnected network, despite the low degree of mineralization. This interconnected mineral network prevents the material from collapsing upon drying, while maintaining the intrinsic high porosity of the initial hydrogel network, well in agreement with our previous results. The density gradually increases with incubation time, as shown in Fig. 4b. This finding supports our TGA results that indicate that the degree of mineralization increases during the first four days of incubation while the amount of polymer contained in the composite decreases due to a pH-driven partial dissolution of the gelatin. Yet, even after 4 days of mineralization, the density reaches values around 0.9 g/cm³, which is far below the density of calcite of 2.71 g/cm³ [73], suggesting that the generated composite is porous. Indeed, granular structures typically possess microporosity arising from the voids present between jammed microgels [64,69]. To test if this is the case in our composite, we perform scanning electron microscopy (SEM) imaging on mineralized samples as a function of the mineralization time. All visualized samples possess pores with diameters up to 300 μm compatible with the expected internal microporosity of granular materials, as shown in Fig. 4c. To quantify the internal porosity of samples that have been mineralized for 4 days, we perform micro computed tomography (μCT) on them. 2D slices and 3D reconstructions confirm a degree of porosity of 47 vol %, as shown in Fig. 4d, Fig. 4e and Movie M2. This porosity is below the value we calculate from the measured density of 67 vol%. We assign this difference to the spatial resolution of the μCT that is limited to 1 μm, which prevents us from detecting smaller pores. This comparison indicates that our composites possess a significant fraction of pores with at least one dimension below 1 μm.

The mineralization of our organic scaffolds strongly increases their stiffness and hardness. The extent of the increase in stiffness and hardness depends on the mechanical properties of the CaCO₃ which are a function of its structure [74,75]. To assess the structure of the CaCO₃ formed in our scaffolds, we perform X-ray diffraction (XRD) as a function of the mineralization time. Samples that have been mineralized for 24 h contain a mixture of vaterite and calcite, as shown in the XRD traces in Fig. 5a. The coexistence of the two phases is confirmed by SEM where we see the sphere-like structure characteristic for vaterite and the cubes, characteristic for calcite, as shown in Fig. 5a. As the incubation time increases, the intensity of the calcite peak grows at the expense of that of the vaterite peak. After four days of incubation, the intensity ratio of calcite to vaterite, measured through XRD, increases 8-fold, as summarized in Fig. 5b.

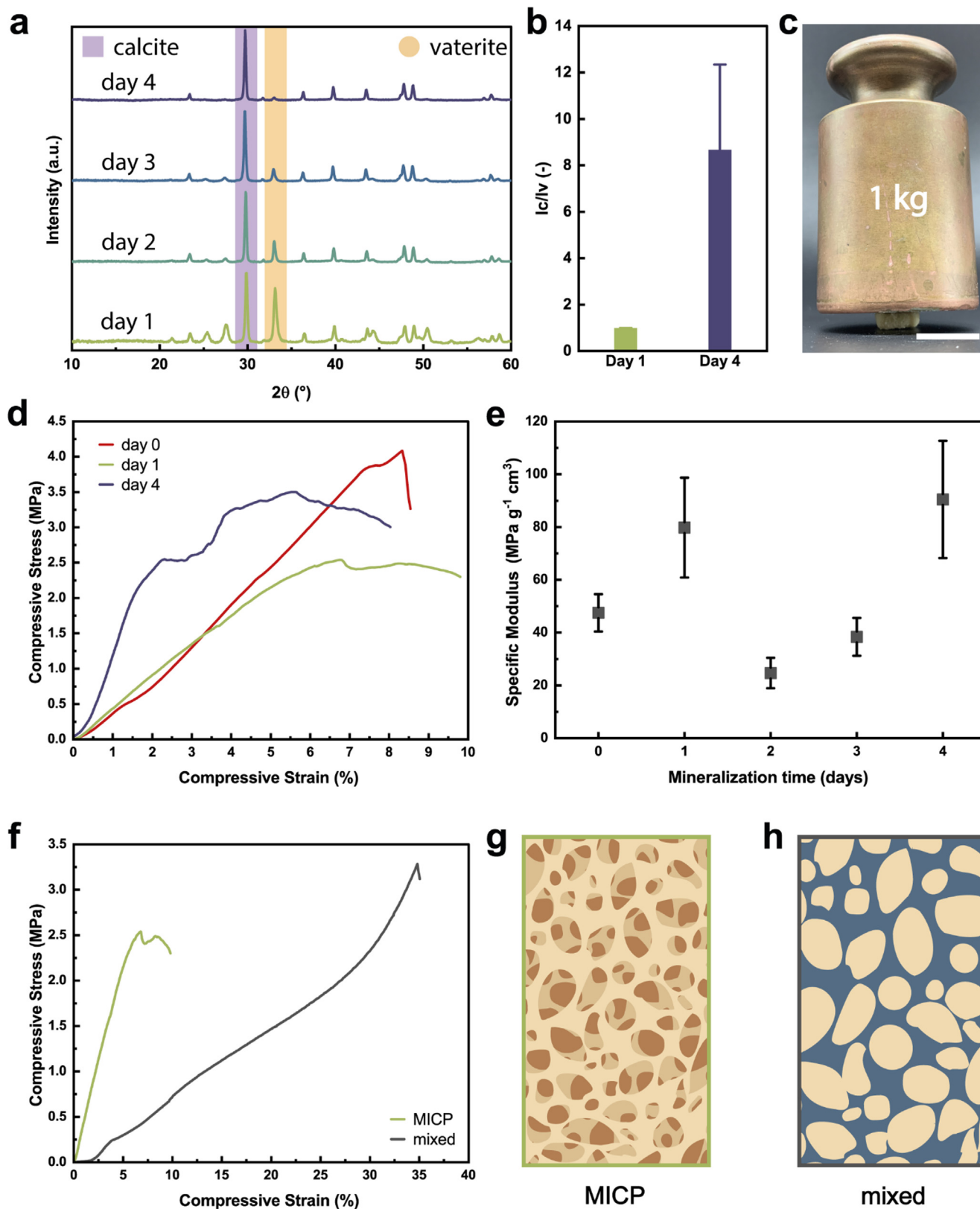
The CaCO₃ polymorph that is formed through the MICP reaction depends on the metabolic activity of the bacteria [76]. Our XRD results suggest that the metabolic activity in the first 24 h is moderate and strongly increases thereafter. To test this suggestion, we quantify the metabolic activity of our 3D printed bacteria, by measuring the bacterial growth within individually

dispersed microgels through optical density measurements (OD600; the optical density is directly correlated to bacteria enzymatic activity) [39,46]. Indeed, within the first 24 h, bacteria display a relatively low activity, that increases over time, as shown in Fig. S6. We assign the low bacteria activity within the first 24 h to the thawing and encapsulation process that might stress the bacteria, limiting their full metabolic activity. This result is in excellent agreement with our XRD analysis: In the initial dormant state, the MICP favors the precipitation of metastable CaCO₃ crystals, such as vaterite, that require a moderately alkaline environment and less energy to be formed [76]. Upon full metabolic recovery and thanks to the increased alkalinity of the solution, the biomineralization reaction shifts towards the precipitation of the stable polymorph calcite, as shown in Fig. S5b. This change in CaCO₃ structure results in stronger biomineralized scaffolds capable of withstanding significant loads, as exemplified on the photograph in Fig. 5c.

To quantify the impact of the MICP on the compressive strength of our material, we prepare cylindrical samples and test them under uniaxial compression. No significant change in stiffness is observed for samples after 24 h of mineralization compared to the unmineralized polymer, as shown in Fig. 5d. This result indicates that after 24 h of mineralization, we form an interconnected mineral network that can withstand its own weight, yet, this network is fragile such that it becomes defective as soon as it is compressed. By contrast, after 4 days of mineralization, the mineral network is sufficiently robust for a cross-section of 50 mm² to bear loads up to 175 N under compression. This behavior results in a compressive stiffness of the composite of 95 MPa, a value that is 3-fold higher than that of unmineralized counterparts, as shown in Fig. 5d.

The mechanical behavior of porous materials depends on their density [77]. To account for the variable porosities of our samples, we normalize the compressive moduli with the sample density. While the dried polymer has a density close to 1 g/cm³, the samples that have been mineralized for 24 h encompass a significant fraction of pores. Hence, the normalization of the compressive modulus with the porosity yields an increase in specific modulus of the sample after 24 h of mineralization with respect to the pure polymer counterpart, as shown in Fig. 5e. Samples incubated for 2–3 days display a sudden drop in mechanical performance, despite their relatively low density, as shown in Fig. 5e. This can be explained by the pH-dependent gelatin degradation which results in loose mineralized fragments that do not bear any load, yet, that contribute to the density of the composite. As a result, the overall specific stiffness of the structure is lowered. As the MICP continues, more and more mineral is precipitated and load-bearing mineral bridges are formed while loose gelatin diffuses out of the material. As a result of this evolution, the specific modulus of the composite increases up to 90 MPa·g⁻¹·cm³ after 4 days of mineralization.

To benchmark the MICP process with conventional composites created by mixing reactants in bulk, we premix our initial gel formulation with 75 wt% of inorganic CaCO₃ filler. As expected, premixed samples prepared in bulk are much softer than the composite that has been biomineralized *in situ* for 24 h, displaying a compressive stiffness 8 times lower than the mineralized sample, as shown in Fig. 5f. We assign the large dif-



ference in compression moduli to the mineral bridges that form in biomineralized samples which result in an interconnected inorganic network. This interconnected inorganic network increases the stiffness of the composite much more efficiently than individually dispersed fillers present in the bulk sample, as schematically summarized in Fig. 5g and 5h. This result highlights the benefit of combining the granular microgel approach with the MICP process for the fabrication of load-bearing biomineral composites.

To demonstrate the potential of our BactoInk to produce macroscopic load-bearing porous 3D composites in an energy efficient manner, we 3D print a sphinx that we subsequently mineralize. The combination of granular printing and MICP allows the fabrication of 3D printed structures with a high printing resolution and shape fidelity, as shown in Fig. 6a. Additionally, the BactoInk injectability and harmless biomineralization offer a new potential solution for art restoration, as exemplified on a statue that contained a hole. This hole can be filled with the BactoInk and upon mineralization, the defect becomes much less severe, as shown in Fig. 6b. To demonstrate the versatility of our approach, we cast the BactoInk into a mold with the shape of a coral. We first produce a negative mold using a commercial cast formulation and a coral master made of poly(lactic acid). Subsequently, we inject the BactoInk in the mold, stabilize the structure by immersing it in a CaCl_2 solution and transfer the scaffold in the mineralizing solution for 4 days. The final structure is dried resulting in a cm-sized free-standing coral, as shown in Fig. 6c. These results demonstrate the potential of the BactoInk to restore or repair broken or partially degraded natural minerals.

Conclusion

We introduce 3D printable bacteria-loaded microgels that can be converted into macroscopic strong organic/inorganic composites comprising mineral contents up to 93 wt% through an energy-efficient MICP process. The synergistic combination of jammed microgels that enable 3D printing and the MICP produces a light-weight inorganic porous structure that resembles that of many natural materials, such as trabecular bones. Importantly, the formulation exclusively contains nature-derived materials. Thanks to the formation of mineral bridges within the material, the obtained inorganic scaffolds are interconnected, such that

the composites can bear pressures up to 3.5 MPa. The low energy impact of the BactoInk combined with its ability to be 3D printed open up new possibilities to restore defective mineral-based structures or to build synthetic mineral analogues that, thanks to the 3D printability of the ink, possess well-defined structures on the micrometer length scale and above. We envisage the versatility of the processing of this ink combined with its low environmental impact and the excellent mechanical properties of the mineralized materials to open up new possibilities to fabricate lightweight load-bearing composites whose structure, composition, and hence mechanical properties resemble more closely those of natural counterparts than those of current synthetic composites. With additional work especially devoted to testing the biocompatibility of the material, these materials might even have the potential to strengthen partially degraded trabecular bones or to replace broken ones.

Methods

Materials. *Sporosarcina pasteurii* (strain designation ATCC 11859, CCOS), gelatin Type-A from porcine skin (gel strength 300, Sigma-Aldrich, G2500), alginate sodium salt (low viscosity, Sigma-Aldrich, A1112), mineral oil light (Sigma-Aldrich, 330779), Span80 (TCI Chemicals, S0060), phosphate buffered saline (PBS, Gibco), calcium chloride 98%+ (Roth, CN93.1), yeast extract (PanReac, A1552), urea (Sigma-Aldrich, 51456), calcium carbonate 99%+ (Sigma-Aldrich, 239216), and ethanol (Reacto-Lab) are all used as received.

Preparation of bacteria-loaded microgels

To prepare bacteria-loaded gelatin microgels, a PBS solution containing 25 wt% gelatin is prepared and maintained at 37 °C to prevent gelation. Then, 1 wt% of freeze-dried *S. pasteurii* is added to the gelatin solution. The gelatin-*S. pasteurii* solution is emulsified by adding mineral oil with 2 wt% Span80 in a 3:1 volume ratio. The emulsion is gelled at 4 °C for 30 min and then centrifuged at 3000 rpm for 15 minutes at 20 °C (Mega Star 1.6R, VWR) to remove the majority of the oil. To remove the remaining oil and surfactant, the obtained microgels are resuspended in PBS, centrifuged, and the supernatant is discarded. The process is repeated five times. The microgels are stored at -20 °C prior to further use.



FIGURE 5

Phase evolution of CaCO_3 and mechanical analysis of biomineralized BactoInk. **a**, XRD scans of samples as a function of the mineralization time. Over time, the calcite peak, indicated in violet, increases with respect to vaterite peak, indicated in orange. **b**, XRD peak intensity ratio of the peak at 29.7°, characteristic of calcite versus that at 33°, characteristic of vaterite. The intensity ratio increases 8-fold if samples are mineralized for 4 days compared to those mineralized for 1 day. **c**, Photograph of a biomineralized scaffold sustaining a 1 kg weight. Scale bar is 20 mm. **d**, Compression curves of samples as a function of mineralization time. A 3-fold increase in stiffness is measured upon mineralization of samples for 4 days. **e**, Compressive modulus normalized by the sample density, called specific modulus, of biomineralized scaffolds as a function of incubation time. An increase in stiffness with respect to the bare polymer is measured already after 24 h, suggesting the formation of an interconnected inorganic network within this time frame. Between day 1 and 2, a strong decrease in specific modulus is observed. We assign this decrease to the pH-induced gelatin degradation that lowers the specific modulus of the polymer. After 2 days, the mineral content significantly increases, leading to a strong increase in modulus. **f**, Compression curves of MICP (green) versus pre-mixed (grey) composite after 24 h of biomineralization. Schematic representation of **g**, the trabecular structure formed by the MICP process, as suggested by our SEM and μCT results and **h**, the filler-reinforced structure. The MICP process endows the biocomposite with higher mechanical stiffness compared to the bulk mixing with fillers.

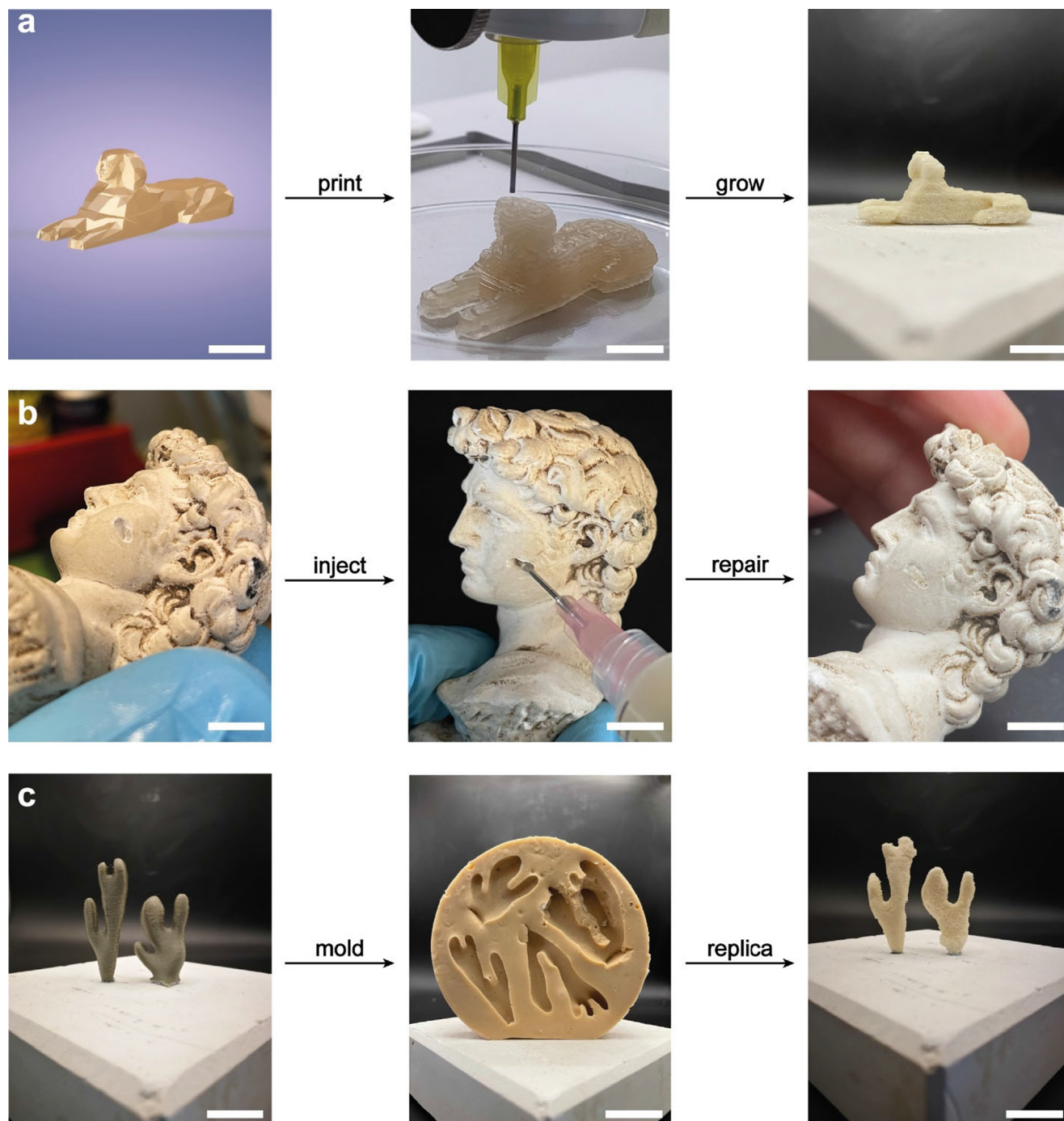


FIGURE 6

Proof of concept of Bactolnk biomineral composites. **a**, 3D printing of Bactolnk into a sphinx. The printed scaffold is biomineralized yielding a hard free-standing object. Scale bar is 20 mm. **b**, Application of Bactolnk as a repairing paste for art restoration. The Bactolnk is injected in a damaged statue and biomineralized to fill the cavity. Scale bar is 10 mm. **c**, Replica molding of corals. The Bactolnk is casted into a negative mold to obtain a biomineralized coral that could be used for reef restoration. Scale bar is 20 mm.

Preparation of Bactolnk

To prepare the Bactolnk, a PBS solution containing 5 wt% alginate is prepared and mixed with the bacteria-loaded microgels at a 4:1 weight ratio. The suspension is centrifuged at 3000 rpm for 15 minutes at 20 °C and the supernatant is discarded. The obtained Bactolnk is stored at –20 °C prior to further use.

3D Printing of Bactolnk

The Bactolnk is loaded in a 3 mL Luer-Lock syringe and trapped air is removed by centrifugation at 3800 rpm for 1 min at 20 °C. 3D printing of Bactolnk is performed with a commercial 3D bio-printer (BIO X, Cellink). The Bactolnk is extruded through a 21 G needle, using a pressure driven piston operated at 70 kPa with a printing speed of 10 mm s⁻¹. Printed samples are gelled in a 1 M CaCl₂ solution for 30 min.

Preparation of molded Bactolnk

To mold-cast the Bactolnk, a negative mold is prepared using Quickform mold making material (Glorex) and a 3D-printed master mold (Prusa MK3S). The Bactolnk is casted in the mold using a syringe and subsequently gelled in a 1 M CaCl₂ solution for 30 min.

Rheology of Bactolnk

Rheology is performed on a DHR-3 TA Instrument with an 8 mm diameter parallel plate steel geometry. All measurements are performed at 25 °C, with an 800 μm gap. Frequency dependent viscosity measurements are made at 0.5% strain. Amplitude sweeps are performed at 1.0 rad s⁻¹ oscillation. Samples are allowed to relax for 200 s at the set temperature before a measurement starts. Rheology is performed on samples with and without bacteria.

Biom mineralization of Bactolnk

Prior to biom mineralization, two aqueous stock solutions containing 1 M CaCl₂ and 1.5 M urea with 0.8 wt% yeast extract are prepared respectively. The two solutions are mixed in a 1:1 volume ratio before use. The gelled Bactolnk sample is added to initiate the biom mineralization. The solution is exchanged every 24 h for four days. After the fourth day, samples are removed from the biom mineralization solution, soaked in ethanol for 30 min, and dried in vacuum at room temperature for 48 h.

Preparation of pre-mixed CaCO₃-hydrogel composite

To obtain a mixed CaCO₃-hydrogel composite, a PBS solution containing 25% w/w gelatin and 75% w/w of CaCO₃ powder is prepared at 37 °C. The obtained solution is mixed with a PBS solution containing 5 wt% alginate. The mixture is centrifuged at 3800 rpm for 15 minutes at 20 °C and the supernatant is discarded. The obtained paste is molded and gelled in a 1 M CaCl₂ containing aqueous solution for 30 min.

TGA measurement of biom mineralized samples

Biom mineralized samples are finely grinded in a mortar before testing with TGA (TGA 4000, PerkinElmer). The measurement is performed from 30 °C to 950 °C at a heating rate of 10 °C min⁻¹ with a nitrogen flow rate of 20 mL min⁻¹. The CaCO₃ weight percentage (wt%_{CaCO₃}) is computed via the following formula:

$$\text{wt}\%_{\text{CaCO}_3} = \frac{\Delta \text{wt}\%}{m_{\text{wCO}_2}} \times m_{\text{wCaCO}_3}$$

Where Δwt% is the weight percentage loss calculated between 600 °C and 900 °C, m_{wCO₂} is the molecular weight of CO₂ (44.102 g mol⁻¹) and m_{wCaCO₃} is the molecular weight of CaCO₃ (100.1 g mol⁻¹). Measured data are representative of at least three independent samples and are reported as mean ± SD.

XRD measurement of biom mineralized samples

XRD analysis (Malvern Panalytical, Empyrean) is performed on biom mineralized powdered samples with 2θ ranging from 10° to 60°, with a scan rate of 0.03° 2θ min⁻¹. The radiation source is Cu Kα with a wavelength of 1.5405 Å and the generator is operated at 40 keV, 40 mA. Baseline removal and peak search is per-

formed using the Peak Analyzer function in OriginPro2021. To evaluate the I_c/I_v ratio, the intensity of the main peak is measured for calcite and vaterite at 29.7° and 33°, respectively. Measured data are representative of at least three independent samples and are reported as mean ± SD.

SEM imaging of biom mineralized samples

SEM imaging is performed on a Zeiss Gemini 300, with a working distance of 6 mm, using a secondary electron detector. Samples are coated with 5 nm of gold.

Optical density measurement of bacteria-loaded microgels

The viability of bacteria after the encapsulation process is assessed by incubating 0.5 g of bacteria-loaded microgels in 50 mL of an aqueous solution containing 0.4 wt% yeast and 0.75 M urea at 30 °C for 4 days. The optical density is measured with a UV-Vis spectrophotometer at a wavelength of 600 nm.

Mechanical characterization of biom mineralized samples

Compressive measurements are performed with a commercial machine (AllroundLine Z005, 5 kN load cell, Zwick Roell). Cylindrical samples are prepared in a silicone mold (d = 8 mm, t = 8 mm) and compressed at a constant velocity of 1.2 mm min⁻¹ until 40% strain is reached. The compressive modulus is calculated as the slope of the initial linear region (from 0% to 1% strain).

μCT imaging and 3D reconstruction of biom mineralized samples

X-Ray μCT is performed with an Ultratom micro tomography system (RX-SOLUTIONS). The sample is scanned at a voxel resolution of 1.05 μm, with a voltage of 45 kV and a current of 166 μA. Amira-Avizo v.2019.4 software is used for reconstruction, segmentation, and visualization.

Data Availability

The raw and processed data required to reproduce these findings are available to download from Zenodo.

Data availability

Data will be made available on request.

Declaration of Competing Interest

The authors declare that they have no known competing financial interests or personal relationships that could have appeared to influence the work reported in this paper.

Acknowledgements

The authors would like to acknowledge Soukaina Ait Said for her help with the rheological experiments. We would also like to thank Mathias Steinacher and Huachuan Du for their helpful and fruitful discussions. The authors would like to thank Pierre Rossi and the Central Environmental Microbiology Laboratory for their help with bacteria handling. We would like to acknowl-

edge Lyesse Laloui for his support. Additionally, Alexandra Clarà Saracho would like to acknowledge the Research Fellowship funded by King's College at the University of Cambridge. The work was financially supported by the Swiss National Centres of Competence in Research (NCCR) Bio-inspired Materials (205603).

Appendix A. Supplementary material

Supplementary information is available in the online version of the paper. Reprints and permissions information is available online at. Correspondence and requests for materials should be addressed to E. A. Supplementary data to this article can be found online at <https://doi.org/10.1016/j.mattod.2023.02.001>.

References

- [1] M. Eder, S. Amini, P. Fratzl, *Science* 362 (2018) 543–547.
- [2] P. Fratzl, R. Weinkamer, *Prog. Mater. Sci.* 52 (2007) 1263–1334.
- [3] J. Sun, B. Bhushan, *RSC Adv.* 2 (2012) 7617–7632.
- [4] C.E. Killian et al., *Adv. Funct. Mater.* 21 (2011) 682–690.
- [5] J.C. Weaver et al., *Science* 336 (2012) 1275–1280.
- [6] H. Du, E. Amstad, *Angew. Chem. Int. Ed.* 59 (2020) 1798–1816.
- [7] H. Du, U. Steiner, E. Amstad, *Chimia* 73 (2019), 29–29.
- [8] H.D. Espinosa et al., *Nat. Commun.* 2 (2011) 173.
- [9] J. Gim et al., *Nat. Commun.* 10 (2019) 4822.
- [10] R. Hsissou et al., *Compos. Struct.* 262 (2021) 113640.
- [11] M.K. Egbo, J. King Saud Univ. - Eng. Sci. 33 (2021) 557–568.
- [12] U.G.K. Wegst et al., *Nat. Mater.* 14 (2015) 23–36.
- [13] G. Mayer, *Science* 310 (2005) 1144–1147.
- [14] M. Hirsch et al., *Biomater. Sci.* (2021).
- [15] X. Dai et al., *J. Polym. Sci. B* 57 (2019) 981–991.
- [16] X.-Y. Liu et al., *ACS Appl. Mater. Interfaces* 11 (2019) 42856–42864.
- [17] T. Magrini et al., *Nat. Commun.* 10 (2019) 2794.
- [18] X. Yang et al., *Cellulose* (2019).
- [19] W. Cui et al., *Matter* 4 (2021) 3646–3661.
- [20] N. Rauner et al., *Nature* 543 (2017) 407–410.
- [21] M. Milovanovic et al., *J. Colloid Interface Sci.* (2020).
- [22] G. Chen et al., *Adv. Funct. Mater.* 32 (2022) 2113262.
- [23] B.Y.S. Kumar et al., *Sci. Rep.* 9 (2019) 1–13.
- [24] Y. Qi et al., *ACS Appl. Mater. Interfaces* 11 (2019) 27598–27604.
- [25] K. Fukao et al., *J. Mater. Chem. B* (2020).
- [26] H. Du et al., *Biomater. Sci.* (2022).
- [27] L.-B. Mao et al., *Science* 354 (2016) 107–110.
- [28] H.-L. Gao et al., *Nat. Commun.* 8 (2017) 287.
- [29] D. Kokkinis, M. Schaffner, A.R. Studart, *Nat. Commun.* 6 (2015) 8643.
- [30] Y. Meng et al., *J. Mater. Chem. B* 8 (2020) 677–690.
- [31] M. Hirsch, A. Charlet, E. Amstad, *Adv. Funct. Mater.* 31 (2021) 2005929.
- [32] A. Charlet et al., *Small* 18 (2022) 2107128.
- [33] A.K. Mohanty et al., *Science* 362 (2018) 536–542.
- [34] D. Terzis, L. Laloui, *Sci. Rep.* 8 (2018) 1416.
- [35] A. Clarà Saracho, S.K. Haigh, M. Ehsan Jorat, *Géotechnique* 71 (2021) 1135–1149.
- [36] H.M. Jonkers et al., *Ecol. Eng.* 36 (2010) 230–235.
- [37] S. Gupta, H.W. Kua, S.D. Pang, *Cem. Concr. Compos.* 86 (2018) 238–254.
- [38] J.T. DeJong et al., *Ecol. Eng.* 36 (2010) 197–210.
- [39] A.C. Saracho et al., *J. Mater. Chem. A* 9 (2021) 24438–24451.
- [40] E. Ortega-Villamagua, M. Gudiño-Gomezjurado, A. Palma-Cando, *Molecules* 25 (2020) 5499.
- [41] T. Hata et al., *J. Nat. Gas Sci. Eng.* 81 (2020) 103490.
- [42] S.S. Bang, J.K. Galinat, V. Ramakrishnan, *Enzyme Microb. Technol.* 28 (2001) 404–409.
- [43] A. Rodrigo-Navarro et al., *Nat. Rev. Mater.* 6 (2021) 1175–1190.
- [44] D. Wangpraseurt et al., *Adv. Funct. Mater.* 32 (2022) 2202273.
- [45] S. Maharjan et al., *Matter* 4 (2021) 217–240.
- [46] M. Schaffner et al., *Sci. Adv.* 3 (2017) eaao6804.
- [47] A. Xin et al., *Adv. Mater.* 33 (2021) 2006946.
- [48] J.E. Mealy et al., *Adv. Mater.* 30 (2018) 1705912.
- [49] C.B. Highley et al., *Adv. Sci.* 6 (2019) 1801076.
- [50] J.M. de Rutte, J. Koh, D. Di Carlo, *Adv. Funct. Mater.* (2019) 1900071.
- [51] L.-C. Gerhardt, A.R. Boccacini, *Materials* 3 (2010) 3867–3910.
- [52] W. Ghach et al., *J. Mater. Chem. B* 1 (2013) 1052–1059.
- [53] S. Xin et al., *Biomater. Sci.* 7 (2019) 1179–1187.
- [54] A.S. Caldwell et al., *Adv. Healthc. Mater.* 6 (2017) 1700254.
- [55] M. Steinacher et al., *ACS Appl. Mater. Interfaces* 13 (2021) 15601–15609.
- [56] B. Kessel et al., *Adv. Sci.* 7 (2020) 2001419.
- [57] B. Miller et al., *Sci. Eng.* 7 (2021) 4164–4174.
- [58] W. Liu et al., *Adv. Healthc. Mater.* 6 (2017) 1601451.
- [59] W. Jia et al., *Biomaterials* 106 (2016) 58–68.
- [60] D. Chimene, R. Kaunas, A.K. Gaharwar, *Adv. Mater.* 32 (2020) 1902026.
- [61] R. Levato et al., *Adv. Mater.* 32 (2020) 1906423.
- [62] A. Charlet, F. Bono, E. Amstad, *Chem. Sci.* 13 (2022) 3082–3093.
- [63] A.C. Daly, M.D. Davidson, J.A. Burdick, *Nat. Commun.* 12 (2021) 753.
- [64] A.C. Daly et al., *Nat. Rev. Mater.* (2019) 1–24.
- [65] D.R. Griffin et al., *Nat. Mater.* 14 (2015) 737–744.
- [66] V.G. Muir et al., *ACS Biomater Sci. Eng.* (2021).
- [67] D.J. Schupp et al., *Chem. Commun.* 55 (2019) 4913–4916.
- [68] W. Chen et al., *Adv. Mater.* 32 (2020) 1907413.
- [69] L. Riley, L. Schirmer, T. Segura, *Curr. Opin. Biotechnol.* 60 (2019) 1–8.
- [70] A. Schwab et al., *Chem. Rev.* 120 (2020) 11028–11055.
- [71] E. Mekonnen et al., *Int. J. Microbiol.* 2021 (2021) e8888641.
- [72] M. Gioffrè et al., *J. Bioact. Compat. Polym.* 27 (2012) 67–77.
- [73] O.K. DeFoe, A.H. Compton, *Phys. Rev.* 25 (1925) 618–620.
- [74] R. Ševčík, P. Šašek, A. Viani, *J. Mater. Sci.* 53 (2018) 4022–4033.
- [75] N.K. Dhama, A. Mukherjee, M.S. Reddy, *Ecol. Eng.* 94 (2016) 443–454.
- [76] A. Clarà Saracho et al., *Sci. Rep.* 10 (2020) 10168.
- [77] O. Coussy, *Mechanics and Physics of Porous Solids*, John Wiley & Sons, 2011.